

Second Harmonic Generation from Metal Nano-Particle Resonators: Numerical Analysis On the Basis of the Hydrodynamic Drude Model

Andreas Hille,^{†,‡} Matthias Moferdt,^{‡,‡} Christian Wolff,^{¶,§} Christian Matyssek,[‡] Rogelio Rodríguez-Oliveros,[‡] Cristopher Prohm,^{||} Jens Niegemann,[⊥] Stefan Grafström,[†] Lukas M. Eng,^{*,†} and Kurt Busch^{‡,¶}

[†]Institut für Angewandte Photophysik, TU Dresden, George-Bähr-Strasse 1, 01069 Dresden, Germany

[‡]AG Theoretische Optik & Photonik, Institut für Physik, Humboldt-Universität zu Berlin, Newtonstrasse 15, 12489 Berlin, Germany

[¶]Max-Born-Institut, Max-Born-Strasse 2A, 12489 Berlin, Germany

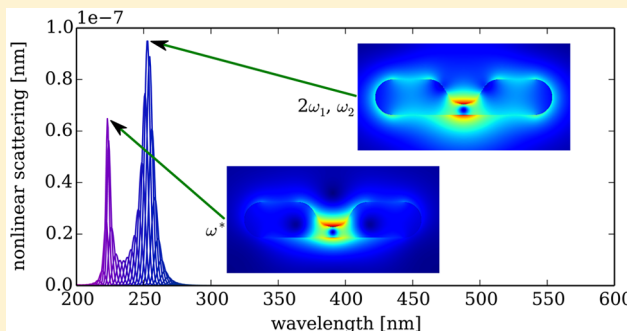
[§]School of Mathematical and Physical Sciences, University of Technology Sydney, NSW 2007 Ultimo, Australia

^{||}Institute of Theoretical Physics, Technische Universität Berlin, Hardenbergstrasse 36, 10623 Berlin, Germany

[⊥]Institute of Electromagnetic Fields (IEF), ETH Zürich, 8092 Zürich, Switzerland

S Supporting Information

ABSTRACT: A detailed computational study of the wavelength-dependent efficiency of optical second-harmonic generation in plasmonic nanostructures is presented. The computations are based on a discontinuous Galerkin Maxwell solver that utilizes a hydrodynamic material model to calculate the free-electron dynamics in metals without any further approximations. Besides wave-mixing effects, the material model thus contains the full nonlocal characteristics of the electromagnetic response, as well as intensity-dependent phenomena such as the Kerr effect. To be specific, two prototypical nanostructures are studied in depth with the help of two independent computer codes. For an infinitely long metal cylinder, it is found that the spectral position of linear particle plasmon modes (dipolar modes, higher-order modes, and, for frequencies above the plasma frequency also bulk plasmon modes) and their associated relative strengths for scattering and absorption both at the fundamental and second-harmonic wavelengths largely control the conversion efficiency. Notably, Fabry–Perot resonances associated with longitudinal bulk plasmons may be detectable via background-free second-harmonic spectroscopy. For a more complex V-groove nanostructure, it becomes possible to engineer a doubly resonant scenario at the fundamental and the second-harmonic wavelength. This leads to an efficient enhancement of second-harmonic emission. Our work thus demonstrates that the careful design of nanostructures on the nonlocal linear level facilitates highly efficient nanoantennas for second-harmonic emission with applications in background-free imaging and frequency conversion systems.



INTRODUCTION

In recent years, nonlinear effects such as second-harmonic generation (SHG) associated with metallic nanoparticles (MNP) have been in the focus of intense investigations.¹ Much of this increased interest is related to the fact that MNPs provide significant field enhancements and are thus promising candidates for ultrahigh-resolution optical microscopy and spectroscopy.² Specifically, the research on point-like light sources that emit at higher harmonics of the fundamental illumination wavelength has gained a lot of attention,^{3–5} as it provides background-free imaging possibilities, i.e., at SHG wavelengths.⁶ Consequently, a major challenge is to find optimized antenna structures that provide a sufficiently strong nonlinear response. For both, our fundamental understanding and design purposes, a reliable way of relating the linear and the nonlinear characteristics of such nanoantennas is highly

desirable. Moreover, a detailed understanding of the basic physical interactions between electromagnetic radiation and metals is beneficial to numerous applications throughout the entire electromagnetic spectrum, i.e., from visible to THz frequencies. In this context, it is worth noting that already at the linear level (spatially) nonlocal material characteristics do lead to resonance shifts and considerably altered field distributions relative to (spatially) local models.^{7–10} In the nonlinear regime, intensity-dependent phenomena such as the Kerr effect could lead to further modifications relative to the linear regime.

To date, numerous techniques for directly simulating the optical properties of MNPs in the time domain such as time-

Received: August 27, 2015

Revised: November 25, 2015

Published: December 15, 2015

dependent density functional theory (TD-DFT),¹¹ the finite-difference time-domain (FDTD) approach,^{12–14} and the discontinuous Galerkin time-domain (DGTD) method^{15,16} have been employed for SHG computations. Clearly, TD-DFT is restricted to treating rather small MNPs only and the incorporation of dissipation and dephasing effects at ambient temperatures is rather challenging.^{11,17} An approach to calculate the nonlinear effects via the macroscopic Maxwell equations using an appropriate material model, such as in the FDTD and the DGTD approach, thus appears much more feasible in order to obtain a quantitative analysis of experimentally relevant systems. In view of its flexible and high-order spatial and temporal discretization,^{18,19} we have chosen to utilize the DGTD method as the Maxwell solver for our subsequent computations. A detailed exposition of the DGTD method can be found in refs 20 and 21. As we shall elaborate below, frequency-domain approaches to the Maxwell equations are also feasible but must be handled with considerable care.

Within macroscopic electrodynamics, the optical properties of metals are generally described by considering the conduction electrons as a plasma that is driven by the Lorentz-force. This fully nonlinear and nonlocal hydrodynamic electron model²² has been successfully used to derive effective $\chi^{(2)}$,^{22,23} and $\chi^{(3)}$ susceptibilities,^{24,25} and more generally, also ponderomotive nonlinearities.^{24,25} Upon linearization, this hydrodynamic model^{7–9} and its recent phenomenological extension¹⁰ allow the computation of a variety of nonlocal effects such as resonance shifts, resonance broadening, effects of bulk plasmon resonances, and the modified field distributions inside and in the immediate vicinity of MNPs. Finally, the hydrodynamic model has recently been applied to simulate the nonlinear response of meta-materials¹⁵ and to study the dispersion relations of propagating surface plasmon polaritons.²⁶

In contrast to the time-domain approach, the alternative frequency-domain approaches compute stationary electromagnetic field distributions via boundary element (BEM) or (volume) finite element (FEM) techniques and rely on the results of perturbation theory that delivers χ^2 parameters as described in refs 27 and 28. These $\chi^{(2)}$ -parameters are then compounded with field distributions at the fundamental wavelength thus providing the second-harmonic response. Clearly, for MNPs these field distributions should generally be computed with a nonlocal linear material model as for instance described in refs 7 and 8. Besides values for the linear material parameters such as damping and plasma frequency, approaches that utilize the perturbative χ^2 method require three additional material parameters that are referred to as the Rudnick–Stern parameters.²⁹ Although these parameters may be derived from the above-described hydrodynamic model via a perturbation theory²² their frequency-dependence still remains a subject of intense debate.^{28,30} In order to predict SHG-responses, further simplifying assumptions are made in practice, such as concentrating only on one specific part of the SHG, i.e., the χ_{nmn} -component,^{27,31} as this is generally assumed to be the dominant contribution. In even further approximations, χ_{nmn} is set to one,²⁷ thus neglecting any frequency dependence and the overall conversion efficiency (albeit the latter can be removed with a scaling factor). However, it should be noted that the two aforementioned assumptions (concentrating on χ_{nmn} and ignoring its dispersion) represent oversimplifications,²⁸ because at least two of the three Rudnick–Stern parameters, and therefore $\chi^{(2)}$ s, are required as fit parameters for obtaining theoretical results which are in agreement with the

experimental findings. Even if these assumptions are not made, a frequency-domain approach still would have to compute the electromagnetic field distribution for a nonlocal material model.

As a result of the above consideration, in the present work, we utilize a “first-principles” hydrodynamic model for the numerical investigation of SHG from MNPs, as this material model contains the full nonlocal and nonlinear response associated with the dynamics of conduction electrons. Specifically, we focus on the correlation between the linear and the nonlinear MNP responses. Given the strong field enhancement effects and the different characteristics of MNP resonances with regards to scattering and absorption, it is important to understand the physical mechanisms that contribute to SHG in MNPs in order to obtain useful design guidelines for applications. First, we study an infinitely long metal nanowire where we find a strong correlation between the linear and nonlinear optical response, which can be assigned to different plasmon resonances of the wire. To elaborate our findings, we also investigate a more complex MNP based on a metal V-groove system. This design is motivated by previous works^{32–34} which predict a strong conversion efficiency when tuning the geometrical parameters of the setup to make it double-resonant, at the fundamental and the second harmonic wavelength.

Throughout, our findings are cross-checked by two independently developed DGTD-codes, one from the Dresden group (group of Prof. Eng) and the other one from the Berlin group (group of Prof. Busch). Both codes deliver results that match very accurately for all cases and both compare very well with an analytical solution for the nonlocal linear case. Specifically, we solve the Maxwell equations for the electromagnetic field and couple them to hydrodynamic Euler equations for the motion of the compressible electron fluid under the influence of the Lorentz force.²² We compute the solutions of this strongly nonlinear set of partial differential equations via the DGTD method^{20,21} both in the linear (weak excitation) and the nonlinear (strong excitation) regime. For details of our numerical procedures and the verification of our two independently developed DGTD codes, including a comparison to a linear nonlocal analytical model, we refer to the [Supporting Information](#).

METHODS

For setting up the simulation, we focus on a simple Drude-model that utilizes the free-electron plasma frequency and damping rate of silver. This choice is made in order to facilitate comparisons with earlier works regarding the nonlocal effects in the linearized version of the hydrodynamic model.^{7,8} Unfortunately, this model excludes the effects of interband-transitions, which are actually important in the wavelength range covered by the fundamental and the SHG signal. These interband contributions can be easily included as described in refs 35 and 36, if necessary. In fact, there also exist several metals, e.g., aluminum,^{9,37} where the interband transitions occur only at frequencies above the plasma-frequency, so that our results are not only theoretically but also practically relevant. Specifically, the above-mentioned comparison considerably enhances the understanding of the underlying physical mechanisms. As a result of this choice, however, the plasma frequency $\omega_p^2 = n_e e^2 / m_e \epsilon_0$ (e , electron charge; ϵ_0 , free space permittivity) of our model is determined by the free electron density n_e and the associated effective electron mass m_e in silver

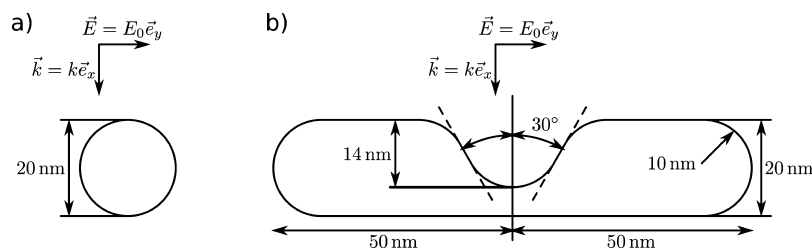


Figure 1. Schematics of the two metal nanoparticle systems used to study SHG generation: (a) a circular metal nanowire of radius $r = 10$ nm and infinite length, and (b) a metal V-groove nanoparticle of infinite length.

and is distinct from the effective plasma frequency of silver which is defined as the zero of the real part of the actual permittivity.

To perform “*ab-initio*” SHG simulations of the metal nanoparticle system, we assume that the quasi-free charge carriers in the metal can be described as an electron fluid (electron density n , current density \vec{j}) that is confined within the nanoparticle by an infinitely high potential well. Consequently, the hydrodynamic Euler equations describe the motion of the compressible electron fluid within the metal, the Thomas-Fermi pressure $p \propto n^{5/3}$ characterizes the electron fluid’s equation of state, while the Maxwell equations describe the electromagnetic fields \vec{E} and \vec{H} . The two subsystems are coupled via the Lorentz-force that drives the compressible electron fluid and, in turn, the fluid’s current density acts as a source for the electromagnetic field.^{22,23} The corresponding equations of motion read as

$$\epsilon \partial_t \vec{E} = \vec{\nabla} \times \vec{H} - q n \vec{v} \quad (1a)$$

$$\mu \partial_t \vec{H} = -\vec{\nabla} \times \vec{E} \quad (1b)$$

$$\partial_t n = -\vec{\nabla} \cdot [n \vec{v}] \quad (1c)$$

$$\begin{aligned} \partial_t [n \vec{v}] = & -\vec{\nabla} \cdot (n \vec{v} \otimes \vec{v}) - \gamma n \vec{v} + \frac{1}{m} \vec{\nabla} p \\ & + \frac{q}{m} n (\vec{E} + \mu \vec{v} \times \vec{H}) \end{aligned} \quad (1d)$$

In the Maxwell equations (eq 1, parts a and b, we have expressed the current density $\vec{j} = q n \vec{v}$ in terms of the electron fluid’s velocity field \vec{v} and the electron charge q . Physically, eq 1c implements the local mass and charge conservation, while the Euler eq 1d represents the conservation of momentum, along with a damping term $\gamma n \vec{v}$, where γ is the damping factor as described below. Furthermore, ϵ and μ denote the dielectric permittivity and the magnetic permeability, respectively. Although ϵ could be any dielectric background permittivity,^{35,36} for a Drude-model, we simply set $\epsilon = \epsilon_0$. In addition, m represents the electron’s effective mass, and the Thomas–Fermi pressure is given by^{22,23}

$$p = \frac{\hbar^2}{5m} (3\pi)^{2/3} n^{5/3} \quad (2)$$

Finally, in order to confine the electron fluid to the nanoparticle, we impose the so-called slip boundary condition, i.e., the normal component of the current density vanishes at the particle’s surface $\vec{n}_{\text{metal}} \cdot \vec{v} = 0$, while electron motion tangential to the particle surface is allowed. To obtain the material parameters for metal, we utilize the fact that the Drude model reflects the linear and spatially local limit of the hydrodynamic model, so that we may fit the data of Johnson

and Christy³⁸ (which has been obtained for rather thick silver films where nonlocal corrections are negligible) using a simple Drude model. Specifically, we obtain a plasma frequency $\omega_p = 1.39 \times 10^{16}$ 1/s and a damping constant $\gamma = 3.23 \times 10^{13}$ 1/s. We use the effective mass value of $m = 0.96 m_e$ (m_e is the free electron mass) as reported by Johnson and Christy,³⁸ which corresponds to an equilibrium electron density within the nanoparticle of $n(t=0) = \epsilon_0 m \omega_p^2 / q^2 = 5.828 \cdot 10^{28} \text{ m}^{-3}$.

To solve the above set of partial differential equations, eq 1, parts a–d, in space and time, we use the discontinuous Galerkin Time-Domain (DGTD) method.^{20,21} The DGTD method features flexible and accurate finite-element spatial discretization via unstructured meshes and high-order polynomial basis functions along with high-order explicit time-stepping schemes. Owing to these features, the DGTD method has become an important workhorse for solving a wide range of nanoplasmonic problems.^{36,39–41}

Since in an ordinary broad-band spectrum the rather small SHG signal is usually hidden under the dominating linear response, we have raster-scanned the spectral behavior of the above-described prototypical plasmonic systems (see Figure 1) with a narrow-band quasi-monochromatic Gaussian pulse of variable center wavelength λ_c and a fixed duration of 13.3 fs. The corresponding peak electric field amplitude was set to 10^6 V/m. We subsequently frequency-filtered the resulting particle response with a discrete Fourier-transform (DFT) filter in order to extract both the linear and the nonlinear signals. Given that the narrow-band excitation has been designed to have nearly no linear contribution at the SHG wavelength, the entire emission that is collected at $\lambda_c/2$ originates from the SHG process, i.e. the signal is background free (the SHG signal is up to 12 orders of magnitude smaller than the maximum amplitude of the incident pulse, for the incident electric field amplitude under consideration).

An infinitely long circular metal nanowire is a particularly simple nanoplasmonic system. Such systems have been thoroughly studied in the linear optical regime, both with local⁴² and nonlocal material models^{7,8} and shall serve us for validating our computational schemes. We use a radius of 10 nm (see Figure 1a). We proceed by exciting the metal nanowire with p-polarized plane-wave pulses as described above, at center wavelengths λ_c varied over a very broad frequency range, thereby covering all the features of the spectrum.

We then move on to a system of increased complexity: a V-groove nanosystem, consisting of an infinite rod of cross section 100 nm by 20 nm with a groove of depth 14 nm (see Figure 1b). Such V-groove systems feature a manifold of linear resonances that are easily adjustable by tuning the groove’s geometrical parameters, hence coupling the linear and nonlinear responses. For the V-groove system shown in 1b), we

also raster-scan the nonlinear response as a function of the excitation center wavelength.

RESULTS AND DISCUSSION

As mentioned, all calculations are performed by raster-scanning the narrow band excitation pulse over a certain frequency range. As a result, we retrieve the complete spectra for the cylindrical metal nanoparticle (see Figure 2a). We cover the range from

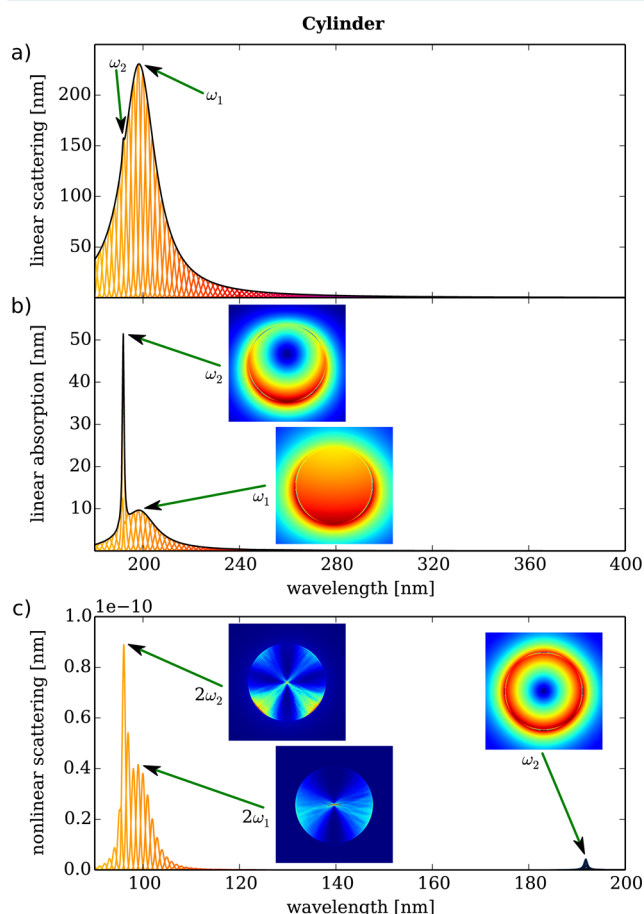


Figure 2. (a) Linear scattering, (b) absorption spectra and (c) nonlinear scattering cross sections from an infinitely long metal nanowire with cylindrical cross-section (radius 10 nm). All quantities are given in units of nm per length and each colored curve represents a single computation with 13.3 fs pulses, centered at different fundamental wavelengths. The envelopes (black) in parts a and b are the well-known linear absorption and scattering cross sections, respectively. Panel c shows the SHG scattering cross-section corresponding to the linear spectra displayed in panels a and b. The SHG spectra exhibit a high degree of similarity with the corresponding linear spectra, notably with the linear absorption cross-section. The insets depict the corresponding near-field images for the prominent resonances. The individual resonances are numbered from longer to shorter wavelengths. Note that all spectra are scaled to the same common value along the axes of the ordinate but have different wavelength axes.

90–400 nm, in steps of 2 nm. We would like to emphasize that in these spectra, every peak corresponds to one full calculation (at λ_c in the linear spectra and at $\lambda_c/2$ in the nonlinear spectra) and is thus depicted with one specific color. The envelope of all these maxima then generates the complete spectrum, nicely reproducing the spectrum that results from a corresponding

broad-band computation, i.e. using a shorter pulse with a width of 1 fs (black curves in Figure 2, parts a and b).

The linear spectra (Figure 2, parts a and b) exhibit the well-known linear plasmon resonances. We number these resonances from longer to shorter wavelengths with ω_1 , ω_2 . We identify the dipole resonance ω_1 at 198 nm and the quadrupole resonance ω_2 at 192 nm for both, the scattering and absorption spectra.

In the SHG-signals (Figure 2c), we identify characteristic resonances as well. These SHG resonances are correlated with the linear resonances in two ways. First, the magnitude of the SHG intensity is large whenever the excitation wavelength of the incident pulse coincides with a plasmon resonance. This is marked with ω_1 in the linear spectra, and results in a strong SHG scattering intensity marked with $2\omega_1$ in Figure 2c. Such a behavior is physically reasonable, since plasmonic resonances often coincide with high field enhancements at the surface of the MNP, and therefore provide a natural way of enhancing the SHG signal, as the SHG generation is proportional to the square of the electric field.

The second and more remarkable correlation occurs, when the SHG wavelength coincides with a linear resonance while the excitation wavelength does not. This is marked with ω_2 in the nonlinear spectra. In such a case, the particle acts as a resonator at the SHG wavelength leading to an increased SHG signal, although the excitation of the incident beam at the fundamental wavelength is off-resonant and practically no field enhancement is present at this wavelength. A similar behavior was suggested in³¹ for coupled metal nanoparticle systems.

An inspection of the corresponding SHG near-field images corroborates the above far-field findings from the SHG spectra. For instance, when taking into account the dephasing due to the incident beam, the near-field patterns for $2\omega_2$ in the nonlinear spectra are similar to those obtained for ω_2 in the linear spectra. Furthermore, the near-field pattern for the $2\omega_1$ resonance exhibits a dipolar behavior and the near-field pattern for the $2\omega_2$ resonance displays a quadrupolar characteristic.

In addition, we find that not only the ordinary particle plasmon resonances but also the (longitudinal) bulk plasmons which arise at frequencies $\omega > \omega_p$ ($\lambda_p \approx 135.5$ nm) have a significant influence on the SHG efficiency (see Figure 3). They lead to additional resonances in the linear spectra and originate from the nonlocal material response.^{7,8} Since bulk plasmons are found at rather short wavelengths and the strengths of the associated resonances are of the order of the estimated SHG signal, an accurate numerical description is required in order to properly resolve the associated effects (see also Supporting Information). As depicted in Figure 3, these plasmons are more prominent in the linear absorption spectra than in the scattering spectra. This leads to modifications of the SHG response that manifest themselves as ripples within the pulses of Figure 3c, and in turn enhances (or suppresses) the SHG by about 10 to 20%.

In order to demonstrate the generality of our approach and to further elaborate our findings we analyze an infinitely long V-groove metal wire (see Figure 1b). Compared to the cylindrical metal nanowire, this system exhibits considerably more complex scattering and absorption characteristics and we display the results in Figure 4. In contrast to the cylindrical nanowire, two main resonances appear when exciting with light polarized along the y -axes (p-polarization). In fact, we have carefully adjusted the geometric parameters such that the first resonance ω_1 occurs at 512 nm while the second one is found

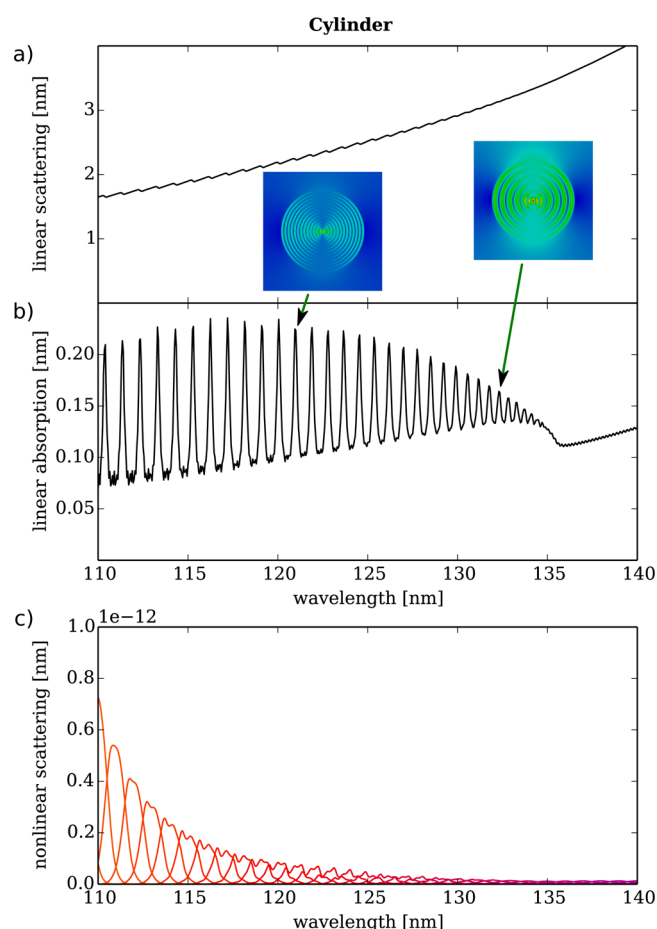


Figure 3. Zoom in on the details of (a) linear scattering, (b) absorption, and (c) nonlinear scattering cross sections from a cylindrical metal nanoparticle (radius 10 nm) for wavelengths in the vicinity and below the plasma frequency. The bulk plasmon resonances, corresponding to Fabry–Perot-like resonances of longitudinal density waves (plasmons) appear only above the plasma frequency. They are most pronounced in the linear absorption spectrum, in the scattering spectrum and the nonlinear spectrum they manifest themselves as smaller ripples. Every curve represents a single simulation. Note that all spectra are scaled to the same common value along the axes of the ordinate and also have the same wavelength axes.

at half the wavelength, i.e., at 256 nm (marked with ω_2). As before, using narrow-band excitation pulses, we scan across the ω_1 -resonance, from 400 to 600 nm. Consequently, we obtain SHG signals around the ω_2 -resonance near 256 nm.

This doubly resonant scenario leads to an enhanced SHG signal that is slightly blue-shifted with respect to ω_2 , to 253 nm (marked with $2\omega_1, \omega_2$ in Figure 4c). In addition, we observe a further SHG resonance at 223 nm (marked with ω^* in Figure 4c) that does not have a counterpart in the linear spectra of Figure 4, parts a and b. While the occurrence of the first SHG resonance ($2\omega_1, \omega_2$) is consistent with our above findings regarding the physical mechanisms of SHG enhancement, additional information is required in order to explain the ω^* SHG resonance. Therefore, we compute linear scattering and absorption cross sections for a V-groove that is rotated by 90° relative to the excitation direction depicted in Figure 1b. In Figure 4, these spectra are shown as dashed lines. This rotated excitation reveals an additional linear resonance exactly at ω^* which is not excited by the first excitation due to symmetry reasons. However, the SHG process is not subject to the

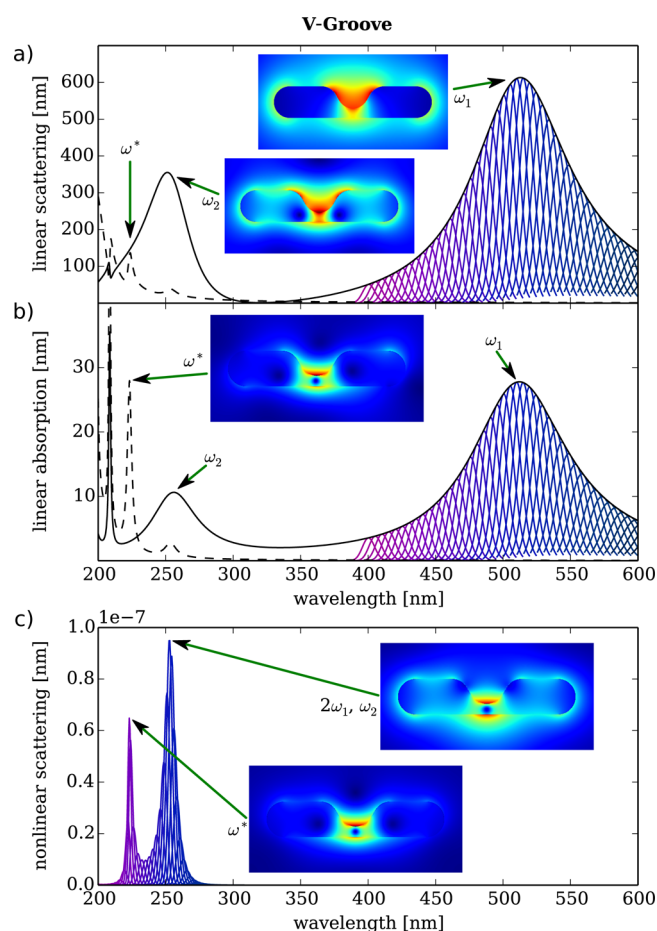


Figure 4. (a) Linear scattering, (b) absorption, and (c) nonlinear scattering cross sections from a metal V-groove system for p-polarized light that is incident perpendicular to the long axis (for details, see Figure 3b). Every curve represents a single computation. In parts a and b, the envelope (black solid line) reproduces exactly the well-known linear cross sections in absorption and scattering. Panel c shows the SHG scattering cross sections corresponding to the linear spectra displayed in panels a and b. The SHG spectra exhibit a high degree of similarity to the corresponding linear spectra. The insets depict the corresponding near-field distribution for the prominent resonances. The individual resonances are numbered from longer to shorter wavelengths. The dashed lines in the linear scattering and absorption spectra are obtained for p-polarized light incident perpendicular to the short axis of the nanoparticle. Note that all spectra are scaled to the same common value along the axes of the ordinate and also have the same wavelength axes. The ordinate scalings are the same as those in Figure 2.

symmetry constraints of linear spectra. Thus, while the resonance at ω^* was not present in the linear spectra for the first excitation direction, it still leads to enhanced SHG. In fact, this behavior is consistent with selection rules described in refs^{31,43}.

This demonstrates that the SHG process is sensitive to all (linear) resonances and not only to those that occur for a specific excitation. Furthermore, the effects described above also suggest that resonances at the second-harmonic wavelength act as effective plasmon resonators. This is backed up by an inspection of the corresponding near-field pattern that we display in Figure 4c: The field distribution for ω^* in the linear spectra is very similar to the field distribution at ω^* in the nonlinear spectra. In addition, we would like to note that these

field distributions are those of the nonlocal hydrodynamic material model and are quite different from those computed from a local Drude model.

We conclude the analysis of the V-groove system by noting that the highest SHG emission is obviously obtained when the system is optimized for best performance, i.e., when the nanoparticle is resonant at both the fundamental and the second-harmonic wavelength. This observation has also been confirmed experimentally by using different arrangements of nanorods in ref 44, and a comparison between Figures 3 and 4 demonstrates that the enhancement can be significant.

CONCLUSIONS

In summary, we have demonstrated that enhancing the second-harmonic response in metallic nanoparticles is closely connected to the alignment of the particles' linear resonances. Our computations show that SHG can be optimized by accounting for the mutual coupling between the linear and second-harmonic optical emission. Best SHG performance may thus be obtained for a doubly resonant scenario where the SHG enhancement can be significant. Moreover, we have also demonstrated that bulk plasmons may become accessible through SHG probing above the plasma frequency. These results have been obtained from an fully nonlocal and nonlinear "ab-initio" hydrodynamic material model for the metal's conduction electrons without any further approximations such as a restriction to specific effective tensor components, i.e., $\chi_{nm}^{(2)}$.

The strong correlation between the SHG characteristics of metal nanoparticles and their linear scattering and absorption cross sections thus provides simple design rules for engineering nanoparticle systems with efficient second-harmonic emission, as required for many nano-optical applications such as background-free spectroscopy, microscopy, and imaging.

ASSOCIATED CONTENT

Supporting Information

The Supporting Information is available free of charge on the ACS Publications website at DOI: 10.1021/acs.jpcc.5b08348.

Separate files for items presented in the pdf (ZIP)
Hydrodynamic equations within the DGTD framework; implementation of hydrodynamic and Maxwell equations; details of the computational study; validation and convergence characteristics; comparison to an analytical reference solution; resolving bulk plasmons; numerical convergence; redundancy of two independent codes; comparison to the local Drude material model (PDF)

AUTHOR INFORMATION

Corresponding Author

*(L.M.E.) E-mail: lukas.eng@iapp.de.

Author Contributions

#These authors contributed equally to this work.

Notes

The authors declare no competing financial interest.

ACKNOWLEDGMENTS

This work was supported by the Target Research Project PLAISIR in the European Union (EU) Framework Program 7 as well as by the Deutsche Forschungsgemeinschaft (DFG) through projects BU 1107/7-2 and BU 1107/8-1. L.M.E.

acknowledges financial support of the Cluster of Excellence "Center of Advancing Electronics Dresden".

REFERENCES

- (1) Kauranen, M.; Zayats, A. V. Nonlinear Plasmonics. *Nat. Photonics* **2012**, *6*, 737–748.
- (2) Kalkbrenner, T.; Håkanson, U.; Sandoghdar, V. Tomographic Plasmon Spectroscopy of a Single Gold Nanoparticle. *Nano Lett.* **2004**, *4*, 2309–2314.
- (3) Jarrett, J. W.; Chandra, M.; Knappenberger, K. L., Jr Optimization of Nonlinear Optical Localization Using Electromagnetic Surface Fields (NOLES) Imaging. *J. Chem. Phys.* **2013**, *138*, 214202.
- (4) Bautista, G.; Huttunen, M. J.; Kontio, J. M.; Simonen, J.; Kauranen, M. Third- and Second-Harmonic Generation Microscopy of Individual Metal Nanocones Using Cylindrical Vector Beams. *Opt. Express* **2013**, *21*, 21918–21923.
- (5) Reichenbach, P.; Horneber, A.; Gollmer, D. A.; Hille, A.; Mihaljevic, J.; Schäfer, C.; Kern, D. P.; Meixner, A. J.; Zhang, D.; Fleischer, M.; Eng, L. M. Nonlinear Optical Point Light Sources Through Field Enhancement at Metallic Nanocones. *Opt. Express* **2014**, *22*, 15484–15501.
- (6) Reichenbach, P.; Eng, L. M.; Georgi, U.; Voit, B. 3D-Steering and Superfocusing of Second-Harmonic Radiation through Plasmonic Nano Antenna Arrays. *J. Laser Appl.* **2012**, *24*, 042005.
- (7) Toscano, G.; Raza, S.; Jauho, A.-P.; Mortensen, N. A.; Wubs, M. Modified Field Enhancement and Extinction by Plasmonic Nanowire Dimers Due to Nonlocal Response. *Opt. Express* **2012**, *20*, 4176–4188.
- (8) Hiremath, K. R.; Zschiedrich, L.; Schmidt, F. Numerical Solution of Nonlocal Hydrodynamic Drude Model for Arbitrary Shaped Nano-Plasmonic Structures Using Nédélec Finite Elements. *J. Comput. Phys.* **2012**, *231* (17), 5890–5896.
- (9) Christensen, T.; Yan, W.; Raza, S.; Jauho, A.-P.; Mortensen, N. A.; Wubs, M. Nonlocal Response of Metallic Nanospheres Probed by Light, Electrons, and Atoms. *ACS Nano* **2014**, *8*, 1745–1758.
- (10) Mortensen, N.; Raza, S.; Wubs, M.; Sondergaard, T.; Bozhevolnyi, S. A Generalized Non-Local Optical Response Theory for Plasmonic Nanostructures. *Nat. Commun.* **2014**, *5*, 3809.
- (11) Marinica, D. C.; Kazansky, A. K.; Nordlander, P.; Aizpurua, J.; Borisov, A. G. Quantum Plasmonics: Nonlinear Effects in the Field Enhancement of a Plasmonic Nanoparticle Dimer. *Nano Lett.* **2012**, *12*, 1333–1339.
- (12) Zeng, Y.; Hoyer, W.; Liu, J.; Koch, S. W.; Moloney, J. V. Classical Theory for Second-Harmonic Generation from Metallic Nanoparticles. *Phys. Rev. B: Condens. Matter Mater. Phys.* **2009**, *79*, 235109.
- (13) Liu, J.; Brio, M.; Zeng, Y.; Zakharian, A. R.; Hoyer, W.; Koch, S. W.; Moloney, J. V. Generalization of the FDTD Algorithm for Simulations of Hydrodynamic Nonlinear Drude Model. *J. Comput. Phys.* **2010**, *229*, 5921–5932.
- (14) Laroche, T.; Baida, F. I.; Van Labeke, D. Three-Dimensional Finite-Difference Time-Domain Study of Enhanced Second-Harmonic Generation at the End of a Apertureless Scanning Near-Field Optical Microscope Metal Tip. *J. Opt. Soc. Am. B* **2005**, *22*, 1045–1051.
- (15) Grynko, Y.; Förster, J.; Meier, T. Application of the Discontinuous Galerkin Time Domain Method to the Optics of Metallic Nanostructures. *AAPP Phys., Math., Nat. Sci.* **2011**, *89*, C1V89S1P041.
- (16) Grynko, Y.; Meier, T.; Linden, S.; Niesler, F. B. P.; Wegener, M.; Förstner, J. Optimal Second-Harmonic Generation in Split-Ring Resonator Arrays. *Proc. SPIE* **2013**, *8623*, 86230L.
- (17) Stella, L.; Zhang, P.; Garcia-Vidal, F. J.; Rubio, A.; Garcia-Gonzalez, P. Performance of Nonlocal Optics When Applied to Plasmonic Nanostructures. *J. Phys. Chem. C* **2013**, *117*, 8941–8949.
- (18) Niegemann, J.; König, M.; Stannigel, K.; Busch, K. High-Order Time-Domain Methods for the Analysis of Nano-Photonic Systems. *Photonics and Nanostructures - Fundamentals and Applications* **2009**, *7*, 2–11.

- (19) Niegemann, J.; Pernice, W.; Busch, K. Simulation of Optical Resonators Using DGTD and FDTD. *J. Opt. A: Pure Appl. Opt.* **2009**, *11*, 114015.
- (20) Hesthaven, J. S.; Warburton, T. Nodal High-Order Methods on Unstructured Grids. *J. Comput. Phys.* **2002**, *181*, 186–221.
- (21) Busch, K.; König, M.; Niegemann, J. Discontinuous Galerkin Methods in Nanophotonics. *Laser Photonics Rev.* **2011**, *5*, 773.
- (22) Sipe, J. E.; So, V. C. Y.; Fukui, M.; Stegeman, G. I. Analysis of Second-Harmonic Generation at Metal Surfaces. *Phys. Rev. B: Condens. Matter Mater. Phys.* **1980**, *21*, 4389–4402.
- (23) Corvi, M.; Schaich, W. L. Hydrodynamic-Model Calculations of Second-Harmonic Generation at a Metal Surface. *Phys. Rev. B: Condens. Matter Mater. Phys.* **1986**, *33*, 3688–3695.
- (24) Kentwell, G.; Jones, D. The Time-Dependent Ponderomotive Force. *Phys. Rep.* **1987**, *145*, 319.
- (25) Ginzburg, P.; Hayat, A.; Berkovitch, N.; Orenstein, M. Nonlocal Ponderomotive Nonlinearity in Plasmonics. *Opt. Lett.* **2010**, *35*, 1551.
- (26) Ginzburg, P.; Krasavin, A. V.; Wurtz, G. A.; Zayats, A. V. Nonperturbative Hydrodynamic Model for Multiple Harmonics Generation in Metallic Nanostructures. *ACS Photonics* **2015**, *2*, 8–13.
- (27) Mäkitalo, J.; Suuriniemi, S.; Kauranen, M. Boundary Element Method for Surface Nonlinear Optics of Nanoparticles. *Opt. Express* **2011**, *19*, 23386.
- (28) Bachelier, G.; Butet, J.; Russier-Antoine, I.; Jonin, C.; Benichou, E.; Brevet, P.-F. Origin of Optical Second-Harmonic Generation in Spherical Gold Nanoparticles: Local Surface and Nonlocal Bulk Contributions. *Phys. Rev. B: Condens. Matter Mater. Phys.* **2010**, *82*, 235403.
- (29) Rudnick, J.; Stern, E. A. Second-Harmonic Radiation from Metal Surfaces. *Phys. Rev. B* **1971**, *4*, 4274–4290.
- (30) Liebsch, A. Second-Harmonic Generation at Simple Metal Surfaces. *Phys. Rev. Lett.* **1988**, *61*, 1233–1236.
- (31) Butet, J.; Dutta-Gupta, S.; Martin, O. J. F. Surface Second-Harmonic Generation from Coupled Spherical Plasmonic Nanoparticles: Eigenmode Analysis and Symmetry Properties. *Phys. Rev. B: Condens. Matter Mater. Phys.* **2014**, *89*, 245449.
- (32) Ashkin, A.; Boyd, G.; Dziedzic, J. Resonant Optical Second Harmonic Generation and Mixing. *IEEE J. Quantum Electron.* **1966**, *2*, 109–124.
- (33) Ou, Z.; Kimble, H. J. Enhanced Conversion Efficiency for Harmonic Generation with Double Resonance. *Opt. Lett.* **1993**, *18*, 1053–1055.
- (34) Liscidini, M.; Andreani, L. C. Second-Harmonic Generation in Doubly Resonant Microcavities with Periodic Dielectric Mirrors. *Phys. Rev. E* **2006**, *73*, 016613.
- (35) Scalora, M.; Vincenti, M. A.; de Ceglia, D.; Roppo, V.; Centini, M.; Akozbek, N.; Bloemer, M. J. Second- and Third-Harmonic Generation in Metal-Based Structures. *Phys. Rev. A: At., Mol., Opt. Phys.* **2010**, *82*, 043828.
- (36) Kullock, R.; Hille, A.; Haußmann, A.; Grafström, S.; Eng, L. M. SHG Simulations of Plasmonic Nanoparticles using Curved Elements. *Opt. Express* **2011**, *19*, 14426–14436.
- (37) Rakic, A. D. Algorithm for the Determination of Intrinsic Optical Constants of Metal Films: Application to Aluminum. *Appl. Opt.* **1995**, *34*, 4755.
- (38) Johnson, P. B.; Christy, R. W. Optical Constants of the Noble Metals. *Phys. Rev. B* **1972**, *6*, 4370–4379.
- (39) Stannigel, K.; König, M.; Niegemann, J.; Busch, K. Discontinuous Galerkin Time-Domain Computations of Metallic Nanostructures. *Opt. Express* **2009**, *17*, 14934–14947.
- (40) Hille, A.; Kullock, R.; Grafström, S.; Eng, L. M. Improving Nano-Optical Simulations Through Curved Elements Implemented within the Discontinuous Galerkin Method. *J. Comput. Theor. Nanosci.* **2010**, *7*, 1581–1586.
- (41) von Cube, F.; Irsen, S.; Diehl, R.; Niegemann, J.; Busch, K.; Linden, S. From Isolated Metaatoms to Photonic Metamaterials: Evolution of the Plasmonic Near-Field. *Nano Lett.* **2013**, *13*, 703.
- (42) Bohren, C. F.; Huffman, D. R. *Absorption and Scattering of Light by Small Particles*; John Wiley & Sons: New York, 1998.
- (43) Park, S.; Hahn, J. W.; Lee, J. Y. Doubly Resonant Metallic Nanostructure for High Conversion Efficiency of Second Harmonic Generation. *Opt. Express* **2012**, *20*, 4856.
- (44) Thyagarajan, K.; Rivier, S.; Lovera, A.; Martin, O. J. F. Enhanced Second-Harmonic Generation from Double Resonant Plasmonic Antennae. *Opt. Express* **2012**, *20*, 12860–12865.